

Qintao Sun, Yan Xiang, Yue Liu, Liang Xu, Tianle Leng, Yifan Ye, Alessandro Fortunelli,*
William A Goddard, III,* and Tao Cheng*

Cite This: *J. Phys. Chem. Lett.* 2022, 13, 8047–8054



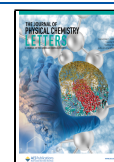
Metrics & More



Supporting Information

Computational modeling has been demonstrated as a powerful tool in studying the SEI to reveal the elementary reactions and atomic structures. Especially, *ab initio* molecular dynamics (AIMD) has been widely applied to investigate SEI reactions in LMB.^{26,27} Meanwhile, quantum mechanism (QM) at the density functional theory (DFT) level can predict core level shifts (CLS) comparable with experimental results.²⁸ Therefore, atomic-based multiscale simulation can provide both atomic details and prediction of XPS CLS.²⁹ XPS prediction links theoretical SEI modeling and experimental SEI reactions and structures. Equipped with XPS prediction, AIMD

Published: August 22, 2022



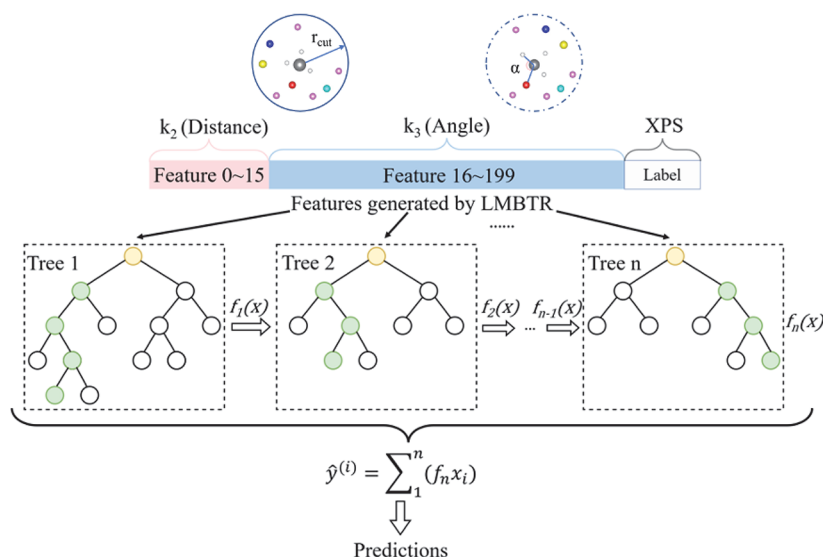


Figure 1. Scheme of XPS prediction using ML model from HAIR simulation.

simulation can fill the gap between experiment and theory, which opens up the deep collaboration between theory and experiment. Thus, experimental data can validate the simulation model. In turn, the validated model can provide reliable information on the SEI atomic structure to guide experiment.³⁰

There are still numerous challenges in multiscale simulation to establish an efficient SEI XPS prediction framework. The first is how to predict the SEI structure. SEI structure prediction has been a difficult problem in simulation. The most commonly used method to predict the reaction mechanism is AIMD. However, AIMD calculations are too expensive to afford brute force simulation for more than a few tens of picoseconds. Such a limited time scale is inadequate for predicting the initial SEI reactions and their structure. In this work, we employed hybrid *ab initio* and reactive molecular dynamics (HAIR) to extend the AIMD time scale. HAIR can boost AIMD simulation by tens to hundreds of times while maintaining DFT precision. The extended time scale is of great help in improving the efficiency and accuracy of SEI prediction.

The second challenge is how to predict the XPS spectra. In addition to the position of XPS peaks, the distribution of XPS is a crucial experimental variable.³¹ Numerous computations are necessary to simulate the XPS distribution.^{27,32} Considering the expensive cost of DFT-based XPS prediction,^{27,30} more efficient methods are needed to achieve large-scale and fast XPS prediction. A well trained machine learning (ML) model can provide an efficient data-driven solution to problems in batteries.^{33–35} For example, Nakayama et al.³⁶ applied an exhaustive search with a Gaussian process (ES-GP) to estimate cation–solvent interaction energies for a series of commonly used organic solvents. They discovered that the most important features to provide reliable predictions are boiling point, dipole moment, and highest occupied molecular orbital (HOMO). Min et al.³⁷ integrated experimental data sets with ML to optimize the parameters of Ni-rich NMC cathode fabrication. After investigating the performance of a variety of ML models, they demonstrated that extreme random trees (ERT) present the best performance with the lowest error. Wang et al.³⁸ developed a partial least-squares (PLS) model to

estimate the volume change of spinel and layered oxides in solid-state electrolytes. Wang et al. established an XGBoost-based ML model that can accurately predict the discharged capacities in doped lithium nickel–cobalt–manganese cathode materials.³⁹ Roman et al. built and analyzed an ML pipeline for assessment of battery capacity fade, a battery health indicator, on 179 cells cycled under varied circumstances.⁴⁰ In recent work, Kireeva and Pervov used a support vector machine (SVM) model to uncover synthesis and electrochemical property connections in Li-rich layered oxide cathodes utilizing experimental data sets.⁴¹ Specifically, Shi et al. first clarified the three main contradictions occurring to the application of machine learning in materials science in 2020, that is, the contradictions between high dimension and small sample, accuracy and usability of models, learning results, and domain knowledge, and then proposed the machine learning method embedded with materials domain knowledge to reconcile these three contradictions.^{42,43} Furthermore, they verified the effectiveness of domain-knowledge-embedded strategy on machine learning for energy materials.⁴⁴ The first proof-of-concept applications for the prediction of valence and core-level spectra are appearing, even though ML is still in its early age.^{45,46} We developed an ML model to predict the XPS spectra in this work.

Overall, we proposed an artificial intelligence *ab initio* (AI-ai) framework to facilitate the SEI structure and its XPS prediction (Figure 1). The specified system simulated is lithium bis(fluorosulfonyl)-imide (LiFSI) in dimethoxyethane (DME) and 1,1,2,2-tetrafluoroethyl-2,2,3,3-tetrafluoropropylether (TTE), a high performance localized high-concentration electrolyte (LHCE) experimentally reported.²⁸ Such an LHCE system exhibits superior device performance by forming a robust SEI and provides sufficient XPS with which to compare to theory.

The hybrid *ab initio* and reactive force field (HAIR) scheme combines AIMD and reactive molecular dynamics (RMD).^{27,32,47} The HAIR scheme can simulate SEI reactions with an accuracy comparable with density functional theory (DFT) while reducing the computational cost by a factor of 10 to 100. The reactive force field (ReaxFF) can handle components, such as mass transfer, that do not require great

computational precision. HAIR is used in this work to simulate the reductive reaction of electrolyte on an anode toward SEI formation. The HAIR simulation starts from 50 cycles with a 10-time acceleration, 0.5 ps AIMD + 5.0 ps RMD in one cycle. The total simulation time for the first 50 cycles is 275 ps. After the first 50 cycles of simulation, the reactions significantly decrease due to the consumption of reactants. Thus, the acceleration rate is increased to 100-times for another 50 cycles. Each cycle has 0.5 ps AIMD + 50.0 ps RMD. The total simulation time for these 50 cycles is 2525 ps. Overall, the simulation time of HAIR reaches 2.8 ns in 100 cycles.

The CLS calculation is on the level of the PBE-D3 level,^{48,49} with initial state (IS) approximation.²⁹ In IS approximation, CLS is directly calculated by the Kohn–Sham (KS) eigenvalues of the core level ϵ_c and the Fermi energy ϵ_F . Without orbital relaxation, the calculated binding energy value is usually smaller than the absolute experimental value. Nevertheless, the relative binding energy generally agrees well with the experiment results according to our benchmark calculations.^{30,50} Therefore, IS approximation has been proven to be a reliable method, and we chose it to predict the CLS in this work. Using local many-body tensor representation (LMBTR), we converted the structure file of these trajectory frames into a data set of 200 features and 33 000 samples. The CSV file containing all the data is available in supplemental data sheet 1 (in Supporting Information).

The many-body tensor representation (MBTR) can describe both finite and periodic systems.⁵¹ By encoding a structure as a distribution of different structural motifs, MBTR is suitable for applications where the interpretability of the input is important. The mathematics description of MBTR is as follows:

$$f_k(x, z) = \sum_{i=1}^{N_i} w_k(i) \mathcal{D}(x, g_k(i)) \prod_{j=1}^k C_{z_j, Z_{ij}} \quad (1)$$

where x is the coordination, $z \in N^k$ are atomic numbers, $i = (i_1, \dots, i_k) \in \{1, \dots, N_a\}^k$ are index tuples. w_k is a weighting function that weights contributions, for example from far-away atoms. \mathcal{D} is a probability distribution that broadens the probability by using a normal distribution taking g_k as input. Thus, w_k, g_k assign a scalar to k atoms in \mathcal{M} . $C \in \mathbb{R}^{N_a \times N_a}$ is an element correlation matrix. Canonical choices of g_k for $k = 1, 2, 3, 4$ are atom counts, (inverse) distances, angles, and dihedral angles. The similarity of two molecules is measured by the Euclidean distance between their representation.

A local MBTR (LMBTR) is used in this work. The difference between LMBTR and MBTR is, first, the k_1 term has been removed; second, LMBTR employs the chemical species X (atomic number 0) for the central position, allowing it to encode spatial positions that are not centered at any particular atom. The specific LMBTR implementation in Dscribe is as follows⁵²

$$g_2(\mathbf{R}_l, \mathbf{R}_m) = |\mathbf{R}_l - \mathbf{R}_m| \quad (2)$$

$$g_3(\mathbf{R}_l, \mathbf{R}_m, \mathbf{R}_n) = \cos(\angle(\mathbf{R}_l - \mathbf{R}_m, \mathbf{R}_n - \mathbf{R}_m)) \quad (3)$$

Here, g_2 is the inverse distance, g_3 is the cosine of angle. These scalar values of g_2 and g_3 are then broadened by using kernel density estimation with a Gaussian kernel, leading to the following distributions \mathcal{D}_k ,

$$\mathcal{D}_2^{l,m}(x) = \frac{1}{\sigma_2 \sqrt{2\pi}} e^{-[(x - g_2(\mathbf{R}_l, \mathbf{R}_m))^2] / [2\sigma_2^2]} \quad (4)$$

$$\mathcal{D}_3^{l,m,n}(x) = \frac{1}{\sigma_3 \sqrt{2\pi}} e^{-[(x - g_3(\mathbf{R}_l, \mathbf{R}_m, \mathbf{R}_n))^2] / [2\sigma_3^2]} \quad (5)$$

Taking the exponential weighting functions,

$$w_2^{l,m} = e^{-s_k |\mathbf{R}_l - \mathbf{R}_m|} \quad (6)$$

$$w_3^{l,m,n} = e^{-s_k (|\mathbf{R}_l - \mathbf{R}_m| + |\mathbf{R}_m - \mathbf{R}_n| + |\mathbf{R}_l - \mathbf{R}_n|)} \quad (7)$$

The distribution can be obtained as follows:

$$\text{LMBTR}_2^{Z_1, Z_2}(x) = \sum_l \sum_m^{|\mathcal{Z}_1|, |\mathcal{Z}_2|} w_2^{l,m} \mathcal{D}_2^{l,m}(x) \quad (8)$$

$$\text{LMBTR}_3^{Z_1, Z_2, Z_3}(x) = \sum_l \sum_m \sum_n^{|\mathcal{Z}_1|, |\mathcal{Z}_2|, |\mathcal{Z}_3|} w_3^{l,m,n} \mathcal{D}_3^{l,m,n}(x) \quad (9)$$

Benchmark calculations show that higher order terms have negligible improvements in accuracy but significantly increase the computational cost. Thus, only g_2 and g_3 terms are included, and their parameters are listed in Table S1. This setting leads to 200 features for each entry. Through LMBTR, we converted the structure file of these trajectory frames into a data set of 200 features and 33 000 samples. The CSV file containing all the data is available in supplemental data sheet 1 (in Supporting Information).

In this work, we focus on predicting the binding energy of C_{1s} . Due to the rich chemical reactions of SEI, carbon species have the most diversity and are the most valuable to study. Such diversity also ensures that C_{1s} has sufficient training data. For example, 1000 HAIR trajectories can produce 33 000 training sets. Second, the chemical environment in SEI coupled with the various bonding states of the C atom is exceedingly complex. If an accurate prediction of the C element can be reached, the prediction of other elements is straightforward, following the same procedure.

The ML models in this work are implemented based on Scikit-learn (SKlearn) and Tensorflow. Linear regression (LR), random forest (RF), and extreme gradient boosting (XGBoost)⁵³ models are based in SKlearn. An artificial neural network (ANN) is based on Tensorflow. A homemade python code is used for ML training and prediction. This code is available in the Supporting Information. Data preprocessing and principal component analysis (PCA) of the data set are carried out in SKlearn. We divided the original data set into a training set and a test set, with a ratio of 7:3.

Mean absolute error (MAE), root means square error (RMSE), and coefficient of determination (R^2) are used to evaluate the performance of the ML predictions. More details of the simulation methods and models are in the Supporting Information.

A 2.8 ns HAIR simulation was carried out to simulate the initial reactions of primitive SEI formation. Figure 2a shows the initial structure, and 2b shows the final structure after 2.8 ns HAIR simulation. A significant amount of reactions occur during the HAIR simulation. Important reactions include the anion self-sacrificing reaction when the FSI^- reductive decomposes to release F^- . F-rich TTE also reacts with Li by releasing F^- . Because both FSI^- and TTE supply F^- , the amount of LiF is enough to form a distinctive LiF layer. This leads to a LiF-rich inorganic inner layer (IIL). After

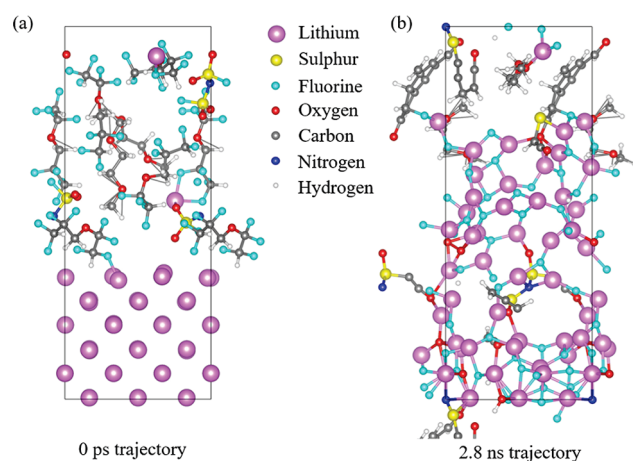


Figure 2. (a) Initial atomic structure of lithium anode of LHCE electrolytes; (b) SEI structure after 2.8 ns HAIR simulation. Color code: lithium, purple; oxygen, red; carbon, gray; fluorine, cyan; sulfur, yellow; nitrogen, blue; hydrogen, white.

defluorination, the TTE backbone is highly unsaturated, accumulating to form organic oligomers via radical initiated chain reactions. Such highly elastic organic oligomers form the organic outer layer (OOL). This inorganic–organic mixed SEI provides the architecture of a robust SEI.

The training set is generated from 5 ps AIMD simulation after HAIR simulation. One thousand snapshots were selected from the AIMD trajectory, and the XPS of C_{1s} are calculated on the DFT level. For each C atom, LMBTR is employed to convert its local environment to features in the form of a 1d entry. In each entry, the first 16 features represent bond distances, and the rest of the features represent three-body angle terms. The label for fitting is the XPS binding energy of C_{1s} predicted from DFT. Four ML algorithms are applied, linear regression (LR), random forest (RF), extreme gradient boosting (XGBoost), and artificial neural network (ANN). The parameters of these four ML models are listed in Table S2.

The criteria to judge the model is 0.1 eV, the experiment detection limit. Table 1 compares the performances of these

Table 1. Evaluation Metrics (R^2 , MAE, RMSE) Value on the Four Machine Learning Models

| ML model | | R^2 (%) | MAE (eV) | RMSE (eV) |
|----------|-------|-----------|----------|-----------|
| LR | Train | 95.04 | 0.22 | 0.28 |
| | Test | 95.09 | 0.22 | 0.27 |
| ANN | Train | 96.81 | 0.16 | 0.20 |
| | Test | 96.76 | 0.14 | 0.17 |
| RF | Train | 99.98 | 0.01 | 0.02 |
| | Test | 99.89 | 0.02 | 0.04 |
| XGBoost | Train | 99.99 | 0.01 | 0.01 |
| | Test | 99.87 | 0.03 | 0.04 |

four ML models. The MAE of both LR and ANN are larger than 0.1 eV, indicating poor performance. Instead, the performance of the two tree models, RF and XGBoost, is satisfactory. As shown in Table 1 and Figure 3, the MAE of RF is less than 0.02 eV in both the training and test sets. MAE of XGBoost is less than 0.02 eV in both the training and test sets. Although MAE is almost the same, the overall performance of XGBoost is better if its small variance is considered. Instead,

jumping points can be seen in RF as shown in Figure 3, although the overall R^2 and RMSE are small. Overall, the above comparison shows that XGBoost has the best performance.

XGBoost is also better for saving training time. The time required to train the ANN model is the longest, which takes more than 70 min using one NVIDIA V100 GPU. Instead, RF only takes ~ 3 min using one Intel Xeon Gold 6226R processor. The training of XGBoost only takes 40 s using one Intel Xeon Gold 6226R processor. Therefore, XGBoost also has the advantage of shortening training overload.

Figure 4 shows the results of peak fitting according to the frequency distribution histograms. As illustrated in Figure 4 and Table S3, the ML model can well reproduce the DFT calculated XPS both in the relative shift and intensity. To compare the performance of the ML model in the test set, the original DFT data used for fitting and the ML prediction results were shown in Figure S1. To calculate the distribution of the XPS data, we used an interval of 0.1 eV.

In the initial stage of the reaction, $C(CF_3)$ in the TTE molecule exhibited a distinct XPS peak. As the reaction proceeded, the TTE was continuously defluorinated, the signal of $C(CF)$ was weakened, and the corresponding signal of $C-C$ was enhanced. As can be seen in Figure 4, although the peaks of $C(CF_3)$, $C(CF_2)$, and $C(CF)$ are present, the intensity of the peaks shows that the amount of $C(CF_3)$ is extremely small, while the amount of $C(CF_2)$ and $C(CF)$ is large. The above results again prove that the intensity of XPS is important information in determining the reaction. Because we can predict the distribution of XPS simultaneously, the predicted results can be directly compared with the experimental values. The comparison results are shown in Figure 4, Figure S2, and Table S3. From the comparison, we can find that the prediction results of ML are almost consistent with the experimental results.

For the visualization and dimensionality reduction of the data, we performed principal component analysis (PCA) on the fitted features of XPS. After the PCA process, the 200 features can be downscaled into 3 dimensions. After dimensionality reduction, the interpretative variance of the data set is 95.58% of the combined variance of the original data set (as shown in Table S3).

Similar to the experiment results, the broad peak generated by simulation consists of contributions from several types of C, which can be further decomposed to explain the underlying physics better. In this work, the C atoms are first classified into several groups according to their local environment based on their chemical structures and PCA Figure 5. Then, multiple Gaussian functions are applied to fit the distributions. This strategy considerably reduces the uncertainties that typically arise during experimentation in the fitting by specifying the peak positions. After the PCA dimensionality reduction, the data aggregates into several major groups, which are identified by different colors as shown in Figure 5. To reveal their atomic structures, typical fragments are highlighted in the inset of Figure 5. Important SEI reaction products include a cyclic $C-C/C-H$ group from TTE defluorination (golden), $C-O/CH_3-O$ group from DME decomposition (blue), $C=O$ group that partially overlaps with $C-O$ (pink), and other TTE decomposition products (green and purple).

The performance of both the RF model and the XGBoost model on a data set with 200 features is promising. After dimension reduction, we predict the data set using the tree models, RF and XGBoost. Table S4 and Figure S3 show the

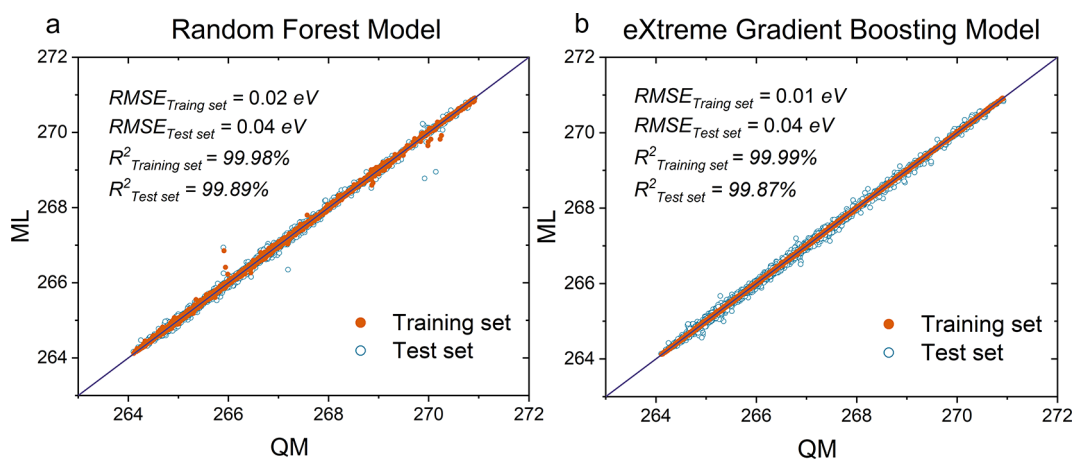


Figure 3. Scatter plots of the training values against the predicted values for the prediction of binding energy by (a) random forest (RF) model and (b) XGBoost model.

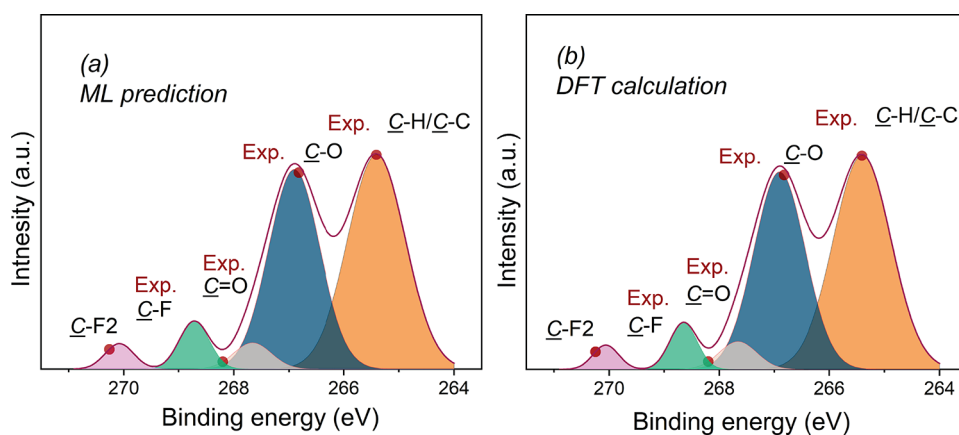


Figure 4. C_{1s} XPS predicted from (a) XGBoost ML model and (b) DFT calculations of LHCE in Li metal anode. Red dots are experimental C_{1s} binding energy shift in LHCE with Li metal anode.²⁸ Different colors are used to distinguish the peaks in XPS.

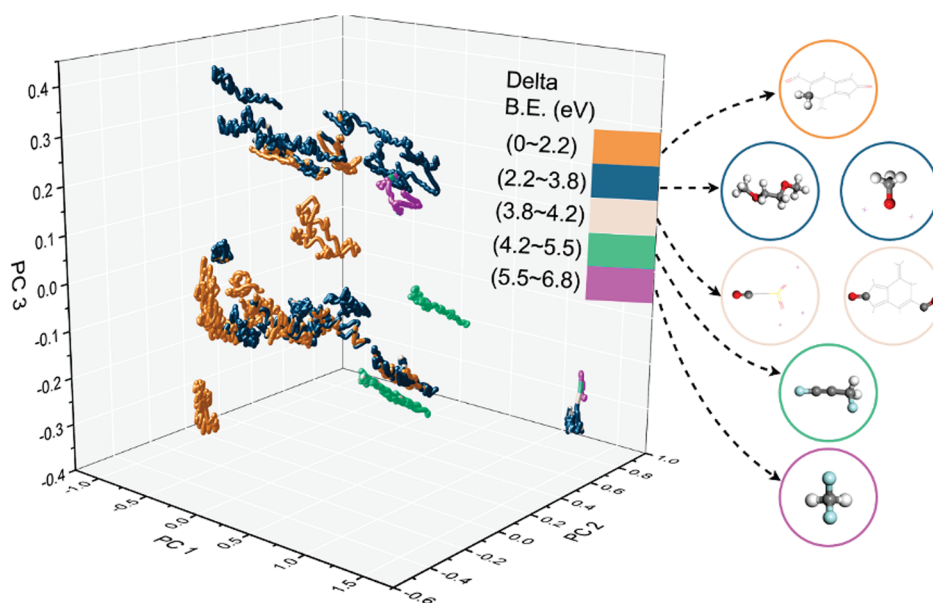


Figure 5. 3D scatter graph with color according to Figure 4 XPS peaks with atomic structures showing on the right side, drawn using the data set of PCA dimensionality reduction.

training results of the data set after dimensionality reduction. When the parameters of the ML model are adjusted, R^2 in the

test set maintains 99.31% accuracy while requiring only 5 s on a personal laptop. Although our research was based on a large

training set, the results indicate that this approach could work with smaller data sets.

Our ML model can be further improved. In the current implementation, only the geometry factors are considered via LMBTR. Other important information, such as atomic charge, can potentially increase the performance. Also, the graph neural network (GNN) is another direction that can increase the transferability of the model.

To summarize, we developed an accurate and efficient AI-ai framework to predict XPS in SEI at marginal cost compared with QM. Such AI-ai framework consists of HAIR simulation to produce the atomic structure of a primitive SEI and a machine learning model to predict XPS. Taking an LHCE with LiFSI+DME+TTE as an example, a HAIR simulation is carried out to simulate initial reactions. After 2.8 ns simulation, the primitive SEI is well developed. XPS predictions on the DFT level were carried out to generate 33 000 training sets from 1000 HAIR snapshots. Four ML models based on LR, ANN, RF, and XGBoost were trained to predict the XPS. Among these four models, XGBoost is the best, with an R^2 of 99.87% and MAE of 0.03 eV. The overall difference between binding energy shift and relative intensity between predicted and calculated values is within ± 0.04 eV. Through PCA dimensionality reduction, the data set can be visualized and clustered. After dimensionality reduction, the RF model still yields an R^2 of 99.31% with the original data set. This work provides a way to reduce the cost of theoretical calculation when performing XPS or other computation-intensive simulations.

■ ASSOCIATED CONTENT

SI Supporting Information

The Supporting Information is available free of charge at <https://pubs.acs.org/doi/10.1021/acs.jpcllett.2c02222>.

HAIR simulation details; Tables S1 to S5; Figures S1 to S3 (PDF)

Source code (TXT)

Original data, and workflow (ZIP)

■ AUTHOR INFORMATION

Corresponding Authors

Alessandro Fortunelli – CNR-ICCOM & IPCF, Consiglio Nazionale delle Ricerche, Pisa 00185, Italy; orcid.org/0000-0001-5337-4450; Email: alessandro.fortunelli@cnr.it

William A Goddard, III – Materials and Process Simulation Center, California Institute of Technology, Pasadena, California 91125, United States; orcid.org/0000-0003-0097-5716; Email: wag@caltech.edu

Tao Cheng – Institute of Functional Nano & Soft Materials (FUNSOM), Jiangsu Key Laboratory for Carbon-Based Functional Materials & Devices, Soochow University, Suzhou, Jiangsu 215123, P. R. China; orcid.org/0000-0003-4830-177X; Email: tcheng@suda.edu.cn

Authors

Qintao Sun – Institute of Functional Nano & Soft Materials (FUNSOM), Jiangsu Key Laboratory for Carbon-Based Functional Materials & Devices, Soochow University, Suzhou 215123 Jiangsu, P. R. China

Yan Xiang – School of Chemistry and Chemical Engineering, Shanghai Jiao Tong University, Shanghai 200240, China

Yue Liu – Institute of Functional Nano & Soft Materials (FUNSOM), Jiangsu Key Laboratory for Carbon-Based Functional Materials & Devices, Soochow University, Suzhou, Jiangsu 215123, P. R. China

Liang Xu – Institute of Functional Nano & Soft Materials (FUNSOM), Jiangsu Key Laboratory for Carbon-Based Functional Materials & Devices, Soochow University, Suzhou, Jiangsu 215123, P. R. China

Tianle Leng – Materials and Process Simulation Center, California Institute of Technology, Pasadena, California 91125, United States

Yifan Ye – National Synchrotron Radiation Laboratory, University of Science and Technology of China, Hefei, Anhui 230026, China

Complete contact information is available at:

<https://pubs.acs.org/doi/10.1021/acs.jpcllett.2c02222>

Notes

The authors declare no competing financial interest.

■ ACKNOWLEDGMENTS

T.C. thanks the Collaborative Innovation Center of Suzhou Nano Science & Technology, the Priority Academic Program Development of Jiangsu Higher Education Institutions (PAPD), the 111 Project, Joint International Research Laboratory of Carbon-Based Functional Materials and Devices, the National Natural Science Foundation of China (21903058 and 22173066), the Natural Science Foundation of Jiangsu Higher Education Institutions (SBK20190810), and the Jiangsu Province High-Level Talents (JNHB-106) for support.

■ REFERENCES

- (1) Goodenough, J. B.; Park, K.-S. The Li-Ion Rechargeable Battery: A Perspective. *J. Am. Chem. Soc.* **2013**, *135*, 1167–1176.
- (2) Dunn, B.; Kamath, H.; Tarascon, J.-M. Electrical Energy Storage for the Grid: A Battery of Choices. *Science* **2011**, *334*, 928–935.
- (3) Dong, T.; Zhang, J.; Xu, G.; Chai, J.; Du, H.; Wang, L.; Wen, H.; Zang, X.; Du, A.; Jia, Q.; Zhou, X.; Cui, G. A multifunctional polymer electrolyte enables ultra-long cycle-life in a high-voltage lithium metal battery. *Energy Environ. Sci.* **2018**, *11*, 1197–1203.
- (4) Winter, M.; Barnett, B.; Xu, K. Before Li Ion Batteries. *Chem. Rev.* **2018**, *118*, 11433–11456.
- (5) Fischer, M.; Werber, M.; Schwartz, P. V. Batteries: Higher energy density than gasoline? *Energy Policy* **2009**, *37*, 2639–2641.
- (6) Lin, D.; Liu, Y.; Cui, Y. Reviving the lithium metal anode for high-energy batteries. *Nat. Nanotechnol.* **2017**, *12*, 194–206.
- (7) Cheng, X.-B.; Zhang, R.; Zhao, C.-Z.; Zhang, Q. Toward Safe Lithium Metal Anode in Rechargeable Batteries: A Review. *Chem. Rev.* **2017**, *117*, 10403–10473.
- (8) Shi, F.; Pei, A.; Boyle, D. T.; Xie, J.; Yu, X.; Zhang, X.; Cui, Y. Lithium metal stripping beneath the solid electrolyte interphase. *Proc. Natl. Acad. Sci. U.S.A.* **2018**, *115*, 8529–8534.
- (9) Wang, Q.; Yao, Z.; Zhao, C.; Verhallen, T.; Tabor, D. P.; Liu, M.; Ooms, F.; Kang, F.; Aspuru-Guzik, A.; Hu, Y.-S.; Wagemaker, M.; Li, B. Interface chemistry of an amide electrolyte for highly reversible lithium metal batteries. *Nat. Commun.* **2020**, *11*, 4188.
- (10) Wu, H.; Jia, H.; Wang, C.; Zhang, J.; Xu, W. Recent Progress in Understanding Solid Electrolyte Interphase on Lithium Metal Anodes. *Adv. Energy Mater.* **2021**, *11*, 2003092.
- (11) Chen, W.-J.; Zhao, C.-X.; Li, B.-Q.; Jin, Q.; Zhang, X.-Q.; Yuan, T.-Q.; Zhang, X.; Jin, Z.; Kaskel, S.; Zhang, Q. A Mixed Ether Electrolyte for Lithium Metal Anode Protection in Working Lithium–Sulfur Batteries. *Energy Environ. Mater.* **2020**, *3*, 160–165.

- (12) Wu, M.; Li, Y.; Liu, X.; Yang, S.; Ma, J.; Dou, S. Perspective on solid-electrolyte interphase regulation for lithium metal batteries. *SmartMat* **2021**, *2*, 5–11.
- (13) Nie, M.; Abraham, D. P.; Chen, Y.; Bose, A.; Lucht, B. L. Silicon Solid Electrolyte Interphase (SEI) of Lithium Ion Battery Characterized by Microscopy and Spectroscopy. *J. Phys. Chem. C* **2013**, *117*, 13403–13412.
- (14) Niehoff, P.; Passerini, S.; Winter, M. Interface Investigations of a Commercial Lithium Ion Battery Graphite Anode Material by Sputter Depth Profile X-ray Photoelectron Spectroscopy. *Langmuir* **2013**, *29*, 5806–5816.
- (15) Wang, H.; Yu, Z.; Kong, X.; Huang, W.; Zhang, Z.; Mackanic, D. G.; Huang, X.; Qin, J.; Bao, Z.; Cui, Y. Dual-Solvent Li-Ion Solvation Enables High-Performance Li-Metal Batteries. *Adv. Mater.* **2021**, *33*, 2008619.
- (16) Song, Y.; Li, X.; He, C. Porous carbon framework nested nickel foam as freestanding host for high energy lithium sulfur batteries. *Chin. Chem. Lett.* **2021**, *32*, 1106–1110.
- (17) Shen, X.; Li, Y.; Qian, T.; Liu, J.; Zhou, J.; Yan, C.; Goodenough, J. B. Lithium anode stable in air for low-cost fabrication of a dendrite-free lithium battery. *Nat. Commun.* **2019**, *10*, 900.
- (18) Chattopadhyay, S.; Lipson, A. L.; Karmel, H. J.; Emery, J. D.; Fister, T. T.; Fenter, P. A.; Hersam, M. C.; Bedzyk, M. J. In Situ X-ray Study of the Solid Electrolyte Interphase (SEI) Formation on Graphene as a Model Li-ion Battery Anode. *Chem. Mater.* **2012**, *24*, 3038–3043.
- (19) Pérez-Villar, S.; Lanz, P.; Schneider, H.; Novák, P. Characterization of a model solid electrolyte interphase/carbon interface by combined in situ Raman/Fourier transform infrared microscopy. *Electrochim. Acta* **2013**, *106*, 506–515.
- (20) Chen, Y.; et al. Hollow CuS Nanoboxes as Li-Free Cathode for High-Rate and Long-Life Lithium Metal Batteries. *Adv. Energy Mater.* **2020**, *10*, 1903401.
- (21) Ju, Z.; Nai, J.; Wang, Y.; Liu, T.; Zheng, J.; Yuan, H.; Sheng, O.; Jin, C.; Zhang, W.; Jin, Z.; Tian, H.; Liu, Y.; Tao, X. Biomacromolecules enabled dendrite-free lithium metal battery and its origin revealed by cryo-electron microscopy. *Nat. Commun.* **2020**, *11*, 488.
- (22) Han, B.; Zhang, Z.; Zou, Y.; Xu, K.; Xu, G.; Wang, H.; Meng, H.; Deng, Y.; Li, J.; Gu, M. Poor Stability of Li_2CO_3 in the Solid Electrolyte Interphase of a Lithium-Metal Anode Revealed by Cryo-Electron Microscopy. *Adv. Mater.* **2021**, *33*, 2100404.
- (23) Li, Y.; Li, Y.; Pei, A.; Yan, K.; Sun, Y.; Wu, C.-L.; Joubert, L.-M.; Chin, R.; Koh, A. L.; Yu, Y.; Perrino, J.; Butz, B.; Chu, S.; Cui, Y. Atomic structure of sensitive battery materials and interfaces revealed by cryo-electron microscopy. *Science* **2017**, *358*, 506–510.
- (24) Wang, J.; Huang, W.; Pei, A.; Li, Y.; Shi, F.; Yu, X.; Cui, Y. Improving cyclability of Li metal batteries at elevated temperatures and its origin revealed by cryo-electron microscopy. *Nat. Energy* **2019**, *4*, 664–670.
- (25) Oswald, S.; Mikhailova, D.; Scheiba, F.; Reichel, P.; Fiedler, A.; Ehrenberg, H. XPS investigations of electrolyte/electrode interactions for various Li-ion battery materials. *Anal. Bioanal. Chem.* **2011**, *400*, 691–696.
- (26) Camacho-Forero, L. E.; Smith, T. W.; Balbuena, P. B. Effects of High and Low Salt Concentration in Electrolytes at Lithium–Metal Anode Surfaces. *J. Phys. Chem. C* **2017**, *121*, 182–194.
- (27) Liu, Y.; Yu, P.; Sun, Q.; Wu, Y.; Xie, M.; Yang, H.; Cheng, T.; Goddard, W. A. Predicted Operando Polymerization at Lithium Anode via Boron Insertion. *ACS Energy Lett.* **2021**, *6*, 2320–2327.
- (28) Ren, X.; et al. Role of inner solvation sheath within salt–solvent complexes in tailoring electrode/electrolyte interphases for lithium metal batteries. *Proc. Natl. Acad. Sci. U.S.A.* **2020**, *117*, 28603–28613.
- (29) Köhler, L.; Kresse, G. Density functional study of CO on Rh(111). *Phys. Rev. B* **2004**, *70*, 165405.
- (30) Yang, H.; Negreiros, F. R.; Sun, Q.; Xie, M.; Sementa, L.; Stener, M.; Ye, Y.; Fortunelli, A.; Goddard, W. A.; Cheng, T. Predictions of Chemical Shifts for Reactive Intermediates in CO₂ Reduction under Operando Conditions. *ACS Appl. Mater. Interfaces* **2021**, *13*, 31554–31560.
- (31) Artyushkova, K.; Kiefer, B.; Halevi, B.; Knop-Gericke, A.; Schlögl, R.; Atanassov, P. Density functional theory calculations of XPS binding energy shift for nitrogen-containing graphene-like structures. *Chem. Commun.* **2013**, *49*, 2539.
- (32) Liu, Y.; Sun, Q.; Yu, P.; Wu, Y.; Xu, L.; Yang, H.; Xie, M.; Cheng, T.; Goddard, W. A. Effects of High and Low Salt Concentrations in Electrolytes at Lithium–Metal Anode Surfaces Using DFT-ReaxFF Hybrid Molecular Dynamics Method. *J. Phys. Chem. Lett.* **2021**, *12*, 2922–2929.
- (33) Jablonka, K. M.; Ongari, D.; Moosavi, S. M.; Smit, B. Big-Data Science in Porous Materials: Materials Genomics and Machine Learning. *Chem. Rev.* **2020**, *120*, 8066–8129.
- (34) Lombardo, T.; et al. Artificial Intelligence Applied to Battery Research: Hype or Reality? *Chem. Rev.* **2022**, *122*, 10899–10969.
- (35) Meuwly, M. Machine Learning for Chemical Reactions. *Chem. Rev.* **2021**, *121*, 10218–10239.
- (36) Nakayama, T.; Igarashi, Y.; Sodeyama, K.; Okada, M. Material search for Li-ion battery electrolytes through an exhaustive search with a Gaussian process. *Chem. Phys. Lett.* **2019**, *731*, 136622.
- (37) Min, K.; Choi, B.; Park, K.; Cho, E. Machine learning assisted optimization of electrochemical properties for Ni-rich cathode materials. *Sci. Rep.* **2018**, *8*, 15778.
- (38) Wang, X.; Xiao, R.; Li, H.; Chen, L. Quantitative structure-property relationship study of cathode volume changes in lithium ion batteries using ab-initio and partial least squares analysis. *J. Materomics* **2017**, *3*, 178–183.
- (39) Wang, G.; Fearn, T.; Wang, T.; Choy, K.-L. Machine-Learning Approach for Predicting the Discharging Capacities of Doped Lithium Nickel–Cobalt–Manganese Cathode Materials in Li-Ion Batteries. *ACS Cent. Sci.* **2021**, *7*, 1551–1560.
- (40) Roman, D.; Saxena, S.; Robu, V.; Pecht, M.; Flynn, D. Machine learning pipeline for battery state-of-health estimation. *Nat. Mach. Intell.* **2021**, *3*, 447–456.
- (41) Kireeva, N.; Pervov, V. S. Materials Informatics Screening of Li-Rich Layered Oxide Cathode Materials with Enhanced Characteristics Using Synthesis Data. *Batter. Supercaps* **2020**, *3*, 427–438.
- (42) Liu, Y.; Guo, B.; Zou, X.; Li, Y.; Shi, S. Machine learning assisted materials design and discovery for rechargeable batteries. *Energy Storage Mater.* **2020**, *31*, 434–450.
- (43) Liu, Y.; Zou, X.; Yang, Z.; Shi, S. Machine Learning Embedded with Materials Domain Knowledge. *J. Chin. Ceram. Soc.* **2022**, *50*, 863–876.
- (44) Zhao, Q.; Avdeev, M.; Chen, L.; Shi, S. Machine learning prediction of activation energy in cubic Li-argyrodites with hierarchically encoding crystal structure-based (HECS) descriptors. *Sci. Bull.* **2021**, *66*, 1401–1408.
- (45) Stuke, A.; Todorović, M.; Rupp, M.; Kunkel, C.; Ghosh, K.; Himanen, L.; Rinke, P. Chemical diversity in molecular orbital energy predictions with kernel ridge regression. *J. Chem. Phys.* **2019**, *150*, 204121.
- (46) Carbone, M. R.; Yoo, S.; Topsakal, M.; Lu, D. Classification of local chemical environments from x-ray absorption spectra using supervised machine learning. *Phys. Rev. Mater.* **2019**, *3*, 033604.
- (47) Liu, Y.; Yu, P.; Wu, Y.; Yang, H.; Xie, M.; Huai, L.; Goddard, W. A.; Cheng, T. The DFT-ReaxFF Hybrid Reactive Dynamics Method with Application to the Reductive Decomposition Reaction of the TFSI and DOL Electrolyte at a Lithium–Metal Anode Surface. *J. Phys. Chem. Lett.* **2021**, *12*, 1300–1306.
- (48) Perdew, J. P.; Burke, K.; Ernzerhof, M. Generalized Gradient Approximation Made Simple. *Phys. Rev. Lett.* **1996**, *77*, 3865–3868.
- (49) Naserifar, S.; Oppenheim, J. J.; Yang, H.; Zhou, T.; Zybin, S.; Rizk, M.; Goddard, W. A. Accurate non-bonded potentials based on periodic quantum mechanics calculations for use in molecular simulations of materials and systems. *J. Chem. Phys.* **2019**, *151*, 154111.
- (50) Taucher, T. C.; Hehn, I.; Hofmann, O. T.; Zharnikov, M.; Zojer, E. Understanding Chemical versus Electrostatic Shifts in X-ray

Photoelectron Spectra of Organic Self-Assembled Monolayers. *J. Phys. Chem. C* **2016**, *120*, 3428–3437.

(51) Huo, H.; Rupp, M. Unified Representation of Molecules and Crystals for Machine Learning. *arXiv* **2017**, No. 1704.06439.

(52) Himanen, L.; Jäger, M. O.; Morooka, E. V.; Federici Canova, F.; Ranawat, Y. S.; Gao, D. Z.; Rinke, P.; Foster, A. S. DScribe: Library of descriptors for machine learning in materials science. *Comput. Phys. Commun.* **2020**, *247*, 106949.

(53) Chen, T.; Guestrin, C. XGBoost: A Scalable Tree Boosting System. Proceedings of the 22nd ACM SIGKDD International Conference on Knowledge Discovery and Data Mining. San Francisco California USA, 2016; pp 785–794.

Recommended by ACS

From Mosaic-Type to Heterojunction-Type SEI Films on the Li Anode: Decoupling Chemical and Electrochemical Degradation of the Electrolyte

Jiaxiang Liu, Jinbao Zhao, *et al.*

JULY 05, 2022

ACS SUSTAINABLE CHEMISTRY & ENGINEERING

READ 

In Situ Visualization of Electrochemical Processes in Solid-State Lithium Batteries

Jing Wan, Li-Jun Wan, *et al.*

AUGUST 16, 2022

ACS ENERGY LETTERS

READ 

In-Depth Characterization of Lithium-Metal Surfaces with XPS and ToF-SIMS: Toward Better Understanding of the Passivation Layer

Svenja-K. Otto, Anja Henss, *et al.*

JANUARY 19, 2021

CHEMISTRY OF MATERIALS

READ 

Li₂O Solid Electrolyte Interphase: Probing Transport Properties at the Chemical Potential of Lithium

Rui Guo and Betar M. Gallant

MAY 28, 2020

CHEMISTRY OF MATERIALS

READ 

Get More Suggestions >